The influence of temperatures on the mechanical properties and fracture behavior of rocks under mixed mode I/II loading

The influence of temperatures on the fracture behavior of rocks under mixed mode I/II loading using digital image correlation

Xunjian Hu[1,2,*], Giuseppe Lacidogna[2], Xiaonan Gong[1]

[1] Research Center of Coastal and Urban Geotechnical Engineering, Zhejiang University, Hangzhou 310058, China

[2]Department of Structural, Geotechnical and Building Engineering, Politecnico di Torino, Corso Duca Degli Abruzzi 24, 10129 Turin, Italy

* Corresponding author: huxunjian2021@zju.edu.cn

Highlights:

1. The mechanical properties and fracture behavior of semi-circular bend samples after high temperature treatment were experimental investigated by three-point bending tests under mixed mode I/II loading.
2. The characteristics of fracture process zone and crack tip opening displacement for pre-heated rocks were determined by digital image correlation technique.
3. Both scanning electron microscopy and polarization microscopy images of fracture morphology reveal the changes in the microstructure of rocks under different temperatures.

Abstract:

A comprehensive understanding of the fracture behavior of pre-heated rocks subjected to mixed mode I/II loading is crucial for deep underground engineering. The effect of high temperature on the fracture process zone (FPZ) and fracture toughness of rocks was experimental investigated using semi-circular bend (SCB) samples. Surface displacement and associated strain field under loading was captured using digital image correlation. The results showed that a gradual decrease in the mechanical properties of SCB samples with increasing temperature. Rocks treated with temperature above 600 °C showed a significant reduction in peak load, generalized stiffness, fracture toughness, and absorbed energy. Moreover, the load-displacement curves and macroscopic fracture characteristics of pre-heated SCB samples exhibited a transition from brittleness to ductility with the increasing temperature under mixed mode I/II loading. Both the FPZ length, width, and the crack tip opening displacement, increased with temperature increase. At lower temperatures (25~400 °C), the ratio of FPZ length to width remains around 2~3, and when the temperature is higher (600~1000 °C), this value increases to 3~4. The initiation of thermally induced cracks in rocks will intensify the damage evolution of rocks under mixed mode I/II loading, as evidenced by the development of the maximum principal strain with displacement. Scanning electron microscopy and polarization microscopy images of microscopic fracture morphology of the pre-heated rocks depicted isolated and dispersed microcracks at lower temperatures, and microcrack networks and broken grains at higher temperatures.

Keywords: High temperature treatment; Digital image correlation; Mixed mode I/II loading; Fracture process zone; Fracture toughness.

1. Introduction

The advancement of sustainable energy has led to an increase in deep underground rock engineering activities, including geothermal exploration from hot dry rock, petroleum and natural gas extraction, and disposal of radioactive nuclear waste [1], [2], [3]. With increasing burial depth, rocks are subjected to higher ground temperatures at a thermal gradient of approximately 0.3 to 0.4 °C/km [4], [5]. For example, bedrocks in underground chambers for nuclear waste disposal may experience temperatures ranging from 100 to 300 °C, with the possibility of further increases during the storage stage [6]. Similarly, the exploration of hot dry rock resources involves temperatures ranging from 150 to 650 °C [1]. Consequently, temperature is a key rule controlling the mechanical properties and fracture behavior of rocks [7]. Moreover, pre-existing microcracks in rocks are susceptible to initiation, propagation, and coalescence under high temperatures, leading to a significant degradation in the bearing capacity of rocks. Therefore, a comprehensive understanding of the effect of temperature on the mechanical properties and fracture behavior of rocks is essential for structural and support design in deep underground rock engineering.

Rock fracture toughness is a fundamental parameter in rock mechanics, quantitatively assessing the ability of rocks to resist original crack extension under different loading conditions. It can be categorized into the in-plane tensile mode (mode I), the in-plane shear mode (mode II), the out-of-plane shear mode (mode III), and their mixed modes (e.g., mixed mode I/II). In order to determine the fracture toughness of rocks in laboratory, different methods were suggested, such as the cracked chevron notched Brazilian disk (CCNBD) method [8] and the semi-circular bend (SCB) method [9]. Many studies have investigated the effect of temperature treatment on mode I fracture toughness of rocks using these methods, revealing a significant reduction in mode I fracture toughness with increasing temperature, particularly above 400 °C [10], [11], [12]. However, some experimental results suggesting a higher temperature threshold of 500~600 °C due to quartz phase transformation [13], [14]. Therefore, the relationship between temperature and fracture toughness is complex, influenced by factors like mineralogical composition, measurement method, loading rate, and sample dimension.

Rock masses often experience complex loading conditions due to random flaw distributions in deep underground rock engineering, the failure of rocks often appears as mixed modes rather than

pure mode I or mode II failures. Hence, studying rock fracture behaviors under mixed mode loading is important. In practice, the mixed mode fracture toughness also changes with temperature, and their relationship is nonlinear and complex [15], [16], [17], [18], [19], [20]. For example, the mixed mode I/II fracture toughness of Kimachi sandstone decreased from room temperature to 75 °C and then increased with temperature between 100 and 200 °C [15]. The mixed mode I/II fracture toughness of sandstone collected from China grew slowly from 20 to 100 °C and reduced gently at 500 °C and then it dropped rapidly between 500 and 600 °C [16]. The aforementioned works primarily focused on the analysis of fracture toughness and macroscopic failure patterns of rocks under mixed mode loading. However, it lacked sufficient analysis of the microcrack behavior of rocks.

The microcracking behavior of rocks under different conditions remains critical for deep underground engineering stability. The technique of digital image correlation (DIC), which is an experimental approach based on tracking the deformation of the rock surface in real-time, has been used to quantitatively investigate the microcracking behavior of rocks [6], [21], [22]. Due to its comprehensive coverage and high precision, this method can be effectively employed to accurately characterize the processes of crack propagation [23]. Moreover, DIC presents notable advantages compared to acoustic emission (AE) for crack length measurement due to its capability to quantify crack length based on full-field strain measurements. Accordingly, it is efficient to investigate the microcrack initiation and propagation mechanism of SCB samples under different conditions by DIC technique [24], [25], [26], [27], [28]. The development of the fracture process zone (FPZ) is mechanistically linked to the damage and failure of quasi-brittle materials, with real-time monitoring of FPZ development crucial for accurate prediction of rock failure [25], [29]. The FPZ is commonly considered as a transition zone from the tip of a propagating macrocrack which has strong discontinuity to the remote region which is assumed to be continuous in micro-scale [30]. DIC results have shown that the crack opening mode of the SCB sandstone samples collected from Chengdu has experienced three stages of slow, linear, and accelerated growth under mode I loading at room temperature [24]. Moreover, the shape of the FPZ of the SCB sample under mode I loading is influenced not only by sample size [24] but also by the temperature conditions [31], [32]. Generally, the length and width of FPZ increase with temperature under mode I loading, while the stress state for microcrack initiation decreases in higher temperature rock samples [32]. Furthermore, the fracture toughness under mode I loading of granite specimens subjected to lower temperatures (e.g.,

25~400 °C) is notably influenced by the presence of FPZ [31].

The attention to FPZ development and associated microcracking behavior in rocks under mixed fracture modes, especially in those subjected to high temperatures, remains insufficient. Most research primarily focuses on FPZ and microcracking behavior in rocks at room temperature under mixed mode loading [33], [34], [35], [36], [37]. Experimental findings suggest that SCB samples can generate mixed mode I/II fractures due to dislocations on the sides of fracture faces [36]. Moreover, sample fractures tend to transition into pure mode I with the extension of microcracks despite initial loading in mixed mode I/II conditions [34]. However, thermally induced cracks in pre-heated SCB samples can influence FPZ development under mixed mode loading conditions, which is notably significant and non-constant [38]. For example, thermally induced cracks may connect, aggregate, and expand around the pre-existing notch tip, ultimately increasing FPZ length, as verified by DIC technique [39]. Thus, DIC technique effectively characterizes FPZ development in rocks during the entire loading process at different temperatures. Nevertheless, the relationship between temperature and FPZ parameters (e.g., width and length) is complex and potentially nonlinear [38]. The evolution of FPZ in rocks after high-temperature treatment has undergone significant changes compared with rocks at room temperature, which deserves further comprehensive study. Specifically, the underlying mechanism of temperature on FPZ development under mixed mode loading remains unclear, with difficulties persisting in understanding fracture behavior of pre-heated rocks in various environments.

To deepen the understanding of the mixed mode I/II fracture characteristics of rocks after high-temperature treatment, three-point bending tests were conducted on pre-heated SCB samples. The mixed mode I/II loadings were achieved by adjusting the inclination angle of the sample notch within six distinct temperature groups (25, 200, 400, 600, 800, and 1000 °C). The DIC method quantitatively analyzed FPZ evolution during the experiment. Key fracture parameters of pre-heated rock samples such as fracture toughness, absorbed energy, and crack tip opening displacement (CTOD) were thoroughly investigated and compared. Finally, to conduct an in-depth analysis of the impact of temperature on the evolution of the FPZ under mixed mode I/II loading, scanning electron microscopy (SEM) and polarization microscopy were employed to observe the micromorphology features of fracture surfaces under elevated temperatures.

2. Experimental methodology

2.1. Rock material and specimen preparation

The rocks investigated in this work were sourced from Shandong Peninsula in China and it exhibits a black-gray color at room temperature. X-ray diffraction (XRD) analysis and mineral content of the rocks are shown in Figs. 1a and 1b, respectively. The rock consists of 83.4% albite, 7.9% biotite, 3.9% quartz, 3.3% microcline, and 1.5% hornblende (Fig. 1b). The rock is classified as fine-grained rock with a holocrystalline texture. To mitigate the potential impact of varying specimen properties on the experiment, SCB samples for this work were extracted from a uniform large rock block. The preparation involved initial creation of cylinder samples, 84.0 mm in diameter and 100.0 mm in height, subsequently fashioned into discs with 84.0 mm diameter and 33.6 mm height using a cutting machine. Following, they were shaped into SCB samples conforming to International Society of Rock Mechanics standards [9]. SCB sample geometry employed in this work aligns with the specifications detailed by Guo and Wong [40]. A straight notch, measuring 21.0 mm in length and 0.7 mm in width, is then introduced to the cut, originating from the center of semi-circular disc. As shown in Fig. 1c, the inclination angle β of the notch of the SCB sample used in this work was 30 ° for mixed mode I/II loading, which is different from Guo and Wong [40].

This work investigated the influence of temperature with six temperature groups (25, 200, 400, 600, 800 and 1000 °C). To minimize additional heat-induced damage to the SCB samples during the heating process, a slow heating rate of 5 °C per minute was applied (Fig. 1d). Once the temperature reached the predetermined value, the SCB samples were subjected to a 4 hours insulation period before cooling to room temperature at the same rate (5 °C/minute). High-temperature treatment was administered using a box-type muffle furnace capable of attaining a maximum temperature of 1200 °C, as depicted in Fig. 1e.

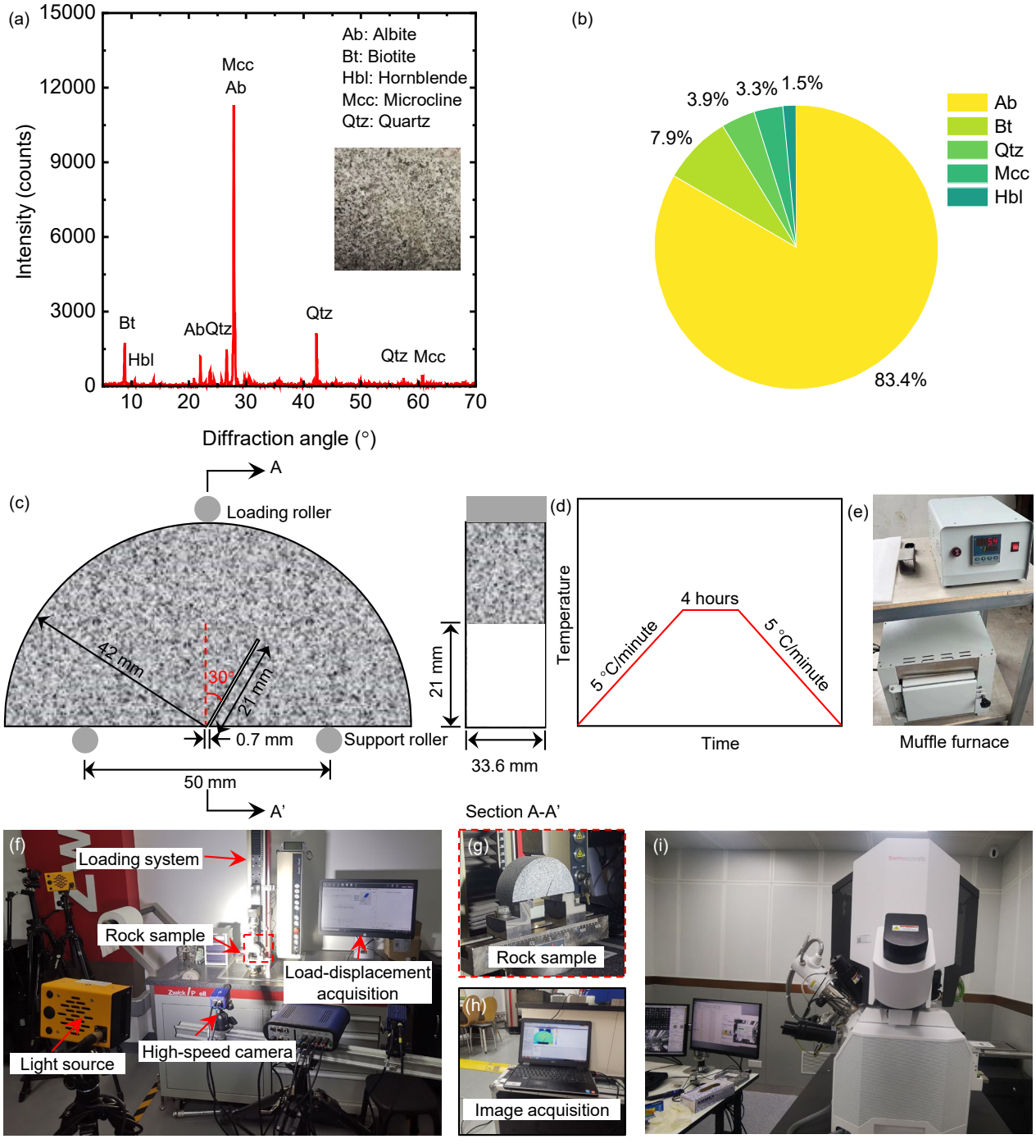

Fig. 1 Mineralogical composition of rock material and experimental study: **a** X-ray diffraction analysis for the rock material; **b** proportion of mineral components; **c** geometry of semi-circular bending sample; **d** heating and cooling paths of SCB samples; **e** muffle furnace; **f** experimental equipments; **g** rock sample undr three-point bending loading; **h** image acquisition system; **i** Thermo Scientific Scios 2 scanning electron microscopy.

2.2. Semi-circular bending (SCB) test

The pre-heated SCB samples were subjected to three-point bending loading on a universal testing

159 machine equipped with a high-speed photographic system (Fig. 1f), which are sourced from the
160 School of Materials Science and Engineering in Zhejiang University. In this experimental
161 arrangement, three small steel rollers were employed for loading the samples (Fig. 1g). The upper
162 steel roller was positioned centrally on the SCB sample, while two lower support steel rollers were
163 symmetrically placed at a span distance of 50 mm (Fig. 1c). A pre-loading of approximately 10 N was
164 applied to stabilize the SCB samples, after which the displacement control mode was initiated at a
165 rate of 0.02 mm/min. The loading system simultaneously monitored the load and displacement of
166 specimens in real time. Upon specimen failure, the testing system promptly ceased loading and
167 recording.

168 In this work, the equation proposed by the International Society of Rock Mechanics was used to
169 calculate the fracture toughness of pre-heated rocks under mixed mode I/II loading. The critical stress
170 intensity factors can be delineated as follows [41]:

171 $$K_{\mathrm{I}} = \frac{P_{\max}}{2RB}\sqrt{\pi a}Y_{\mathrm{I}} \tag{1}$$

172 $$K_{\mathrm{II}} = \frac{P_{\max}}{2RB}\sqrt{\pi a}Y_{\mathrm{II}} \tag{2}$$

173 where K_{I} and K_{II} are mode I and mode II fracture toughness, respectively; $P_{\max}$ is the peak load during
174 the three-point bending test. R and B are the radius and thickness of SCB sample, respectively. The
175 length of notch is a leading from the center of SCB sample. The stress intensity factors Y_{I} and Y_{II} are
176 dimensionless parameters that depend on the sample geometry and loading conditions. In this work,
177 according to the results reported by Ayatollahi and Aliha [41] and Lim et al. [42], the values of Y_{I} and
178 Y_{II} are approximately 2.2390 and 1.3250, respectively.

179 To further reveal the fracture mechanical characteristics of rocks under mixed mode I/II loading,
180 the effective fracture toughness K_{eff} is defined as follows [41]:

181 $$K_{\mathrm{eff}} = \sqrt{K_{\mathrm{I}}^2 + K_{\mathrm{II}}^2} \tag{3}$$

182 The high-speed photographic system (Fig. 1f) comprises a LaVision Imager E-lite high-speed
183 camera, along with a light source and an image acquisition system (Fig. 1h). This high-speed camera,
184 equipped with a charge-coupled device (CCD) boasting a resolution of 1055 × 797 pixels, captured a
185 series of images at a rate of six frames per second. At the onset of the experiments, both the loading
186 and photographic systems were synchronized to commence simultaneously, thereby enabling the
187 real-time recording of mechanical properties and fracture behavior of SCB samples during the mixed

mode I/II loading process.

The Thermo Scientific Scios 2 scanning electron microscopy (Fig. 1i) was utilized to examine the micromorphology features of fracture surfaces of thermally treated SCB samples. The specimens prepared for SEM analysis was coin-shaped, with a diameter of 2.5 mm and a height of 0.5 mm. Additionally, the Leica DM750P polarization microscopy was utilized to investigate the microcrack distribution of specimens after high-temperature treatment.

2.3. Digital image correlation (DIC) technique

The DIC method relies on a unique random texture, represented by speckle patterns on the rock surface. These patterns adhere to the surface of sample and deform along with it during conventional DIC tests [38], [39], ensuring no loss of correlation even under significant deformation. While a manually crafted speckle pattern is typically preferred for optimal accuracy, certain natural materials like wood, rock, sand, and gravel may naturally exhibit distinct inherent speckle patterns [43], [44], [45]. The latter was observed in the case of the fine-grained rock analyzed in this study. As depicted in Fig. 1a, the photograph of rock surface illustrates the natural speckle pattern resulting from the varied minerals in the rock sample. This pattern is characterized by high contrast, indicating a random orientation and a sufficiently large grey spectrum for precise high-strain resolution, as corroborated by the displacement and strain fields obtained through DIC analysis.

The essential principle underlying the DIC technique involves obtaining comprehensive displacement and strain data by analyzing digital images before and after deformation through correlation algorithms. In Fig. 2a, a defined region of interest (ROI) measuring 20 mm in width and 20 mm in height is illustrated. As the SCB specimens were subjected to mixed mode I/II loading conditions, the midpoint of the lower boundary of the ROI and the notch endpoint were not aligned (Fig. 2a). This contrasts with the conventional positioning of the ROI when the SCB specimen subjected to mode I loading conditions [46]. Using a high-speed camera, digital images of the rock surface were obtained during the full loading process. The pre-loading image serves as the reference image, while the image captured during loading represents the deformed state (Fig. 2b). Subsequently, these images are subdivided into numerous subsets (Fig. 2c). As shown in Fig. 2d, a square reference subset centered at point P (x_0, y_0) is selected from the reference image and used to track its corresponding position P' (x_0', y_0') in the deformed image. The deformed displacement components

(Fig. 2e) are obtained by [21]:

$$x_i' - x_i = u_0 + \frac{\partial u}{\partial x}(x_i - x_0) + \frac{\partial u}{\partial y}(y_i - y_0) \tag{4}$$

$$y_i' - y_i = v_0 + \frac{\partial v}{\partial x}(x_i - x_0) + \frac{\partial v}{\partial y}(y_i - y_0) \tag{5}$$

where x_i, y_i, x_i', and y_i' are the coordinate component of points shown in Fig. 2d; u_0 and v_0 are the displacement component of the reference subset center in horizontal and vertical directions; $\frac{\partial u}{\partial x}$, $\frac{\partial u}{\partial y}$, $\frac{\partial v}{\partial x}$, and $\frac{\partial v}{\partial y}$ are the first-order displacement gradient of the reference subset.

The strain components (Fig. 2f) in horizontal and vertical directions can be calculated by:

$$\varepsilon_{xx} = \frac{1}{2}\left[2\frac{\partial u}{\partial x} + \left(\frac{\partial u}{\partial x}\right)^2 + \left(\frac{\partial v}{\partial x}\right)^2\right] \tag{6}$$

$$\varepsilon_{yy} = \frac{1}{2}\left[2\frac{\partial v}{\partial y} + \left(\frac{\partial u}{\partial y}\right)^2 + \left(\frac{\partial v}{\partial y}\right)^2\right] \tag{7}$$

where ε_{xx} and ε_{yy} are the strain components of subset in x and y directions.

The maximum principal strain is defined as the strain occurring in the direction towards the greater deformation [47]. When the SCB specimen is subjected to mixed mode I/II loading, analyzing the changes in the maximum principal strain field is more insightful for revealing the fracture behavior of rocks compared to solely analyzing the strain component in the x direction (ε_{xx}) [34], [48]. Therefore, only the results of the maximum principal strain of ROI are presented (e.g., Fig. 2f). In this study, a commercial software package (DaVis 8.3.0 from LaVision) was utilized to scrutinize the displacement and strain fields of the ROI during the loading process. It is imperative to calibrate the collected digital images to establish their correspondence with the actual SCB sample before conducting the calculations. The calculation parameters during image post-processing are listed as follows: subset: 23, step: 5, subset weights: Gaussian weights, correlation criterion: normalized squared differences.

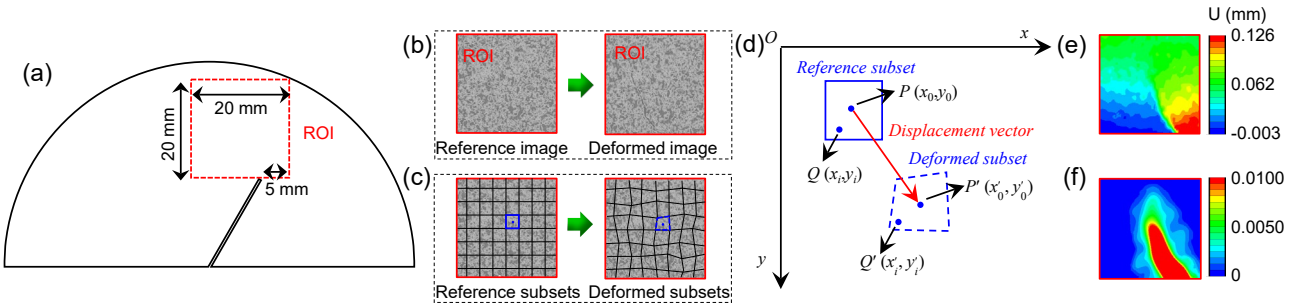

Fig. 2 The process for DIC analysis: **a** the position of ROI; **b** reference and deformed images; **c** reference and deformed subsets; **d** the principles of DIC analysis; **e** horizontal displacement field; **f** maximum principal strain field.

3. Results

3.1. Effect of temperature on the mechanical properties

The load-displacement curves of SCB samples after various high temperature treatments subjected to mixed mode I/II loading are shown in Fig. 3a. At room temperature, untreated SCB samples exhibit obvious brittleness characteristics (Fig. 3a). An initial nonlinear stage is nearly absent, signifying a linear increase in load with displacement until reaching a peak value, followed by a rapid drop, indicating instantaneous loss of bearing capacity and high brittleness. Therefore, the SCB sample at room temperature under mixed mode I/II loading shows a typical load-displacement curve of brittle rock. However, different mechanical behavior is observed when rocks subjected to different high-temperature treatments. From the perspective of macroscopic mechanical properties, both peak load (Fig. 3b) and generalized stiffness (Fig. 3c) decrease gradually with increasing temperature. Consequently, effective fracture toughness (Fig. 3d) of SCB specimens diminishes progressively. For example, when the treatment temperature is increased from 200 to 1000 °C, the effective fracture toughness of SCB samples decreased from 1.085 MPa·m$^{1/2}$ to 0.254 MPa·m$^{1/2}$, a decrease of 76.6%. Moreover, within a 200 °C temperature interval, the most pronounced decline in effective fracture toughness occurs between 400 and 600 °C. Its value decreased from 1.011 MPa·m$^{1/2}$ to 0.554 MPa·m$^{1/2}$, a decrease of 45.2%. This trend is also evident in the load-displacement curve. At lower temperatures (25~400 °C), the load-displacement curves exhibit brittle behavior, with proximately linear and elastic pre-peak stages (Fig. 3a). Conversely, at higher temperatures (600~1000 °C), the load-displacement curves show ductile behavior, characterized by a distinct initial nonlinear stage,

pre-peak hardening stage, and post-peak softening stage (Fig. 3a). While the generalized stiffness remains nearly constant within the 25~400 °C range, it gradually decreases within the 600~1000 °C range (Fig. 3c). This temperature-induced brittle-ductile transition induces significant alterations in the mechanical properties of SCB specimens within the temperature range 400~600 °C. This transition observed in this work is consistent with other experimental results [17], [48], [49], [50]. Especially this temperature range (400~600 °C) also has a significant weakening effect on the effective fracture toughness of rocks, which is an important parameter for the design of deep underground rock engineering.

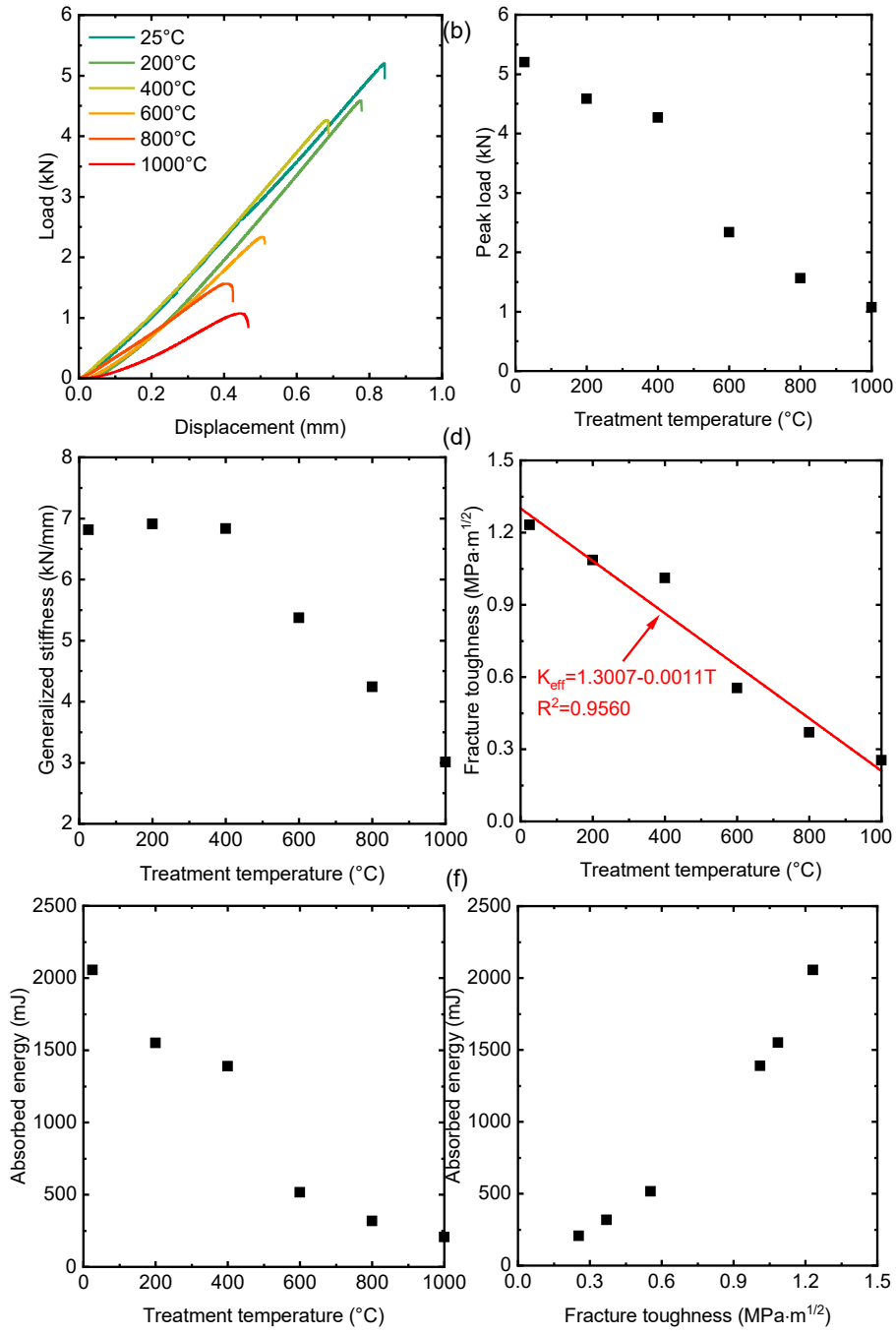

Fig. 3 Mechanical and energy properties of pre-heated SCB samples: **a** load-displacement curves; **b** peak load; **c** generalized stiffness; **d** fracture toughness; **e** absorbed energy of SCB samples; **f** the relationship between absorbed energy and effective fracture toughness.

The damage and microcrack behavior of rocks are accompanied by the absorption, accumulation, and dissipation of energy. Analyzing the energy evolution provides a more comprehensive description of rock mechanical behavior. During the three-point bending test, the SCB sample absorbs energy with increasing load and releases energy upon microcrack initiation and propagation. The area integration method [32], [51] is employed to compute the absorbed energy throughout the mixed mode I/II loading process in this work, utilizing the load-displacement curve of the SCB sample. The absorbed energy before the peak load E_p is calculated as [32]:

$$E_p = \int_0^{d_p} p_i \mathrm{d}d_i \tag{8}$$

where d_p is the displacement corresponding to the peak load; p_i is the load value corresponding to the loading point i; d_i is the displacement of loading point i.

The external load contributes energy to rock failure, which the rock stores as strain energy, while crack propagation consumes this energy, leading to rock damage. The absorbed energy of rocks at different temperatures prior to the peak load during mixed mode I/II loading is shown in Fig. 3e. From an energy point of view, the absorption energy decreases gradually with increasing temperatures. High temperature treatment can cause increased rock original damage before loading tests, and requiring a relatively small amount of energy to propagate microcracks. Under high thermal stress levels, the microstructure of SCB sample gradually loosens, making it easier to form connections between microcracks, which results in a steady decrease in fracture toughness until the brittle-ductile transition is achieved, resulting in failure of the specimen [52], [53]. As shown in Fig. 3f, there exists an almost linear relationship between absorbed energy and fracture toughness of the SCB sample. Higher fracture toughness necessitates greater absorbed energy for rock breakage. This observation is rationalized by the generation of more thermally induced cracks at higher treatment temperatures [54], leading to reduced energy requirements for crack propagation during mixed mode I/II loading. The findings presented in Figs. 3e and 3f underscore a significant correlation between temperature, fracture energy, and fracture toughness, offering valuable insights for the design of deep underground rock engineering. This conclusion aligns well with the experimental results of Feng et al. [51] and

Chen et al. [32], both of whom concluded that the absorption energy of rocks decreases with increased initial thermally induced damage.

3.2. Effect of temperature on the macroscopic fracture characteristics

High-temperature treatment induces notable alterations in both the mechanical properties of SCB specimens (Fig. 3) and the macroscopic fracture characteristics under mixed mode I/II loading conditions. As shown in Fig. 4, at lower temperatures (25~600 °C), the macroscopic fracture progresses from the notch tip to the applied load point between the loading roller and the SCB specimens (Figs. 4a~4d). But at higher temperatures (800~1000 °C), the macroscopic fracture only extends to the upper part of the specimen before terminating (Figs. 4e~4f). This transformation seems to be attributed to the enhanced ductility of the rock after high-temperature treatment, resulting in a reduced crack propagation speed. The experimental results of Alneasan and Alzo'ubi [20] indicated that under mixed mode I/II loading, at a distance of 5 mm from the notch tip and β =30 °, the crack tip speeds are approximately 100~170 m/s and 5~20 m/s at room temperature and 500 °C, respectively. This highlights the significant reduction in crack propagation speed due to high-temperature treatment, a phenomenon associated with the brittle-ductile transition of rocks and energy release (Figs. 3 and 4). In the process of fracture, when the rock sample exhibits brittle behavior, the stored energy is promptly discharged as fractures extend. In contrast, when the rock sample displays ductile behavior, the energy is gradually released, leading to a slower rate of fracture propagation speed. Therefore, in samples subjected to sufficiently high temperature treatments (e.g., 800 °C or 1000 °C), macroscopic fracture fails to propagate fast enough to the boundary of sample when rocks failure.

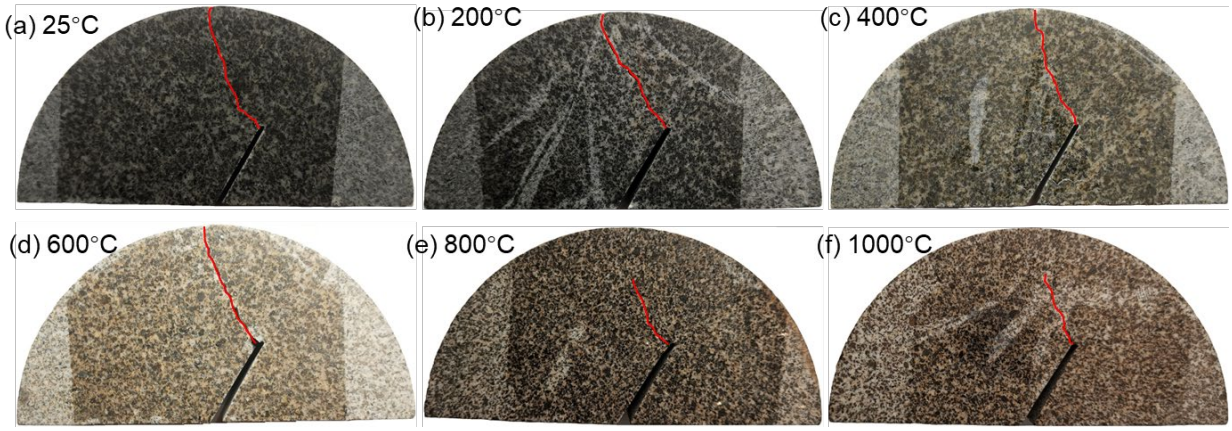

Fig. 4 Macroscopic fracture of SCB samples under different temperatures: **a** 25 °C; **b** 200 °C; **c** 400 °C; **d** 600 °C; **e** 800 °C; **f** 1000 °C. The solid red lines are hand-drawn fractures.

In the examined rock samples of this study, temperature variations appear to exert minimal influence on the macroscopic fracture tortuosity of SCB specimens under mixed mode I/II loading conditions. From a mechanical point of view, in the case of SCB specimens subjected to mixed mode I/II loading (as illustrated in Fig. 1c), fracture propagation typically follows a nonlinear trajectory from the notch tip to the applied load point, a phenomenon supported by numerous experimental findings [16], [36], [48]. This nonlinear trajectory aligns with the path of maximum tangential stress [55], thereby directing fracture growth along a specific route, resulting in comparable macroscopic fracture tortuosity. However, due to the presence of thermally induced microcracks and rock heterogeneity, including microstructural and mechanical heterogeneities, the fracture propagation path may vary among different SCB samples under mixed mode I/II loading, resulting in subtle distinctions in fracture tortuosity among samples treated at different temperatures. Typically, significant deviations in this specific path occur only when the fracture encounters high-strength grains, such as quartz, with extensive areas during propagation [56], [57]. However, the rocks investigated in this study belong to fine-grained rocks, with albite comprising the predominant content (83.4%), possessing lower strength compared to quartz [58], [59]. Hence, the likelihood of substantial deviation in the specific path is relatively low. In summary, high-temperature treatment impacts certain macroscopic fracture characteristics of SCB specimens under mixed mode I/II loading, notably reducing crack propagation speed, but it has little effect on its geometric characteristics like fracture tortuosity.

3.2. Effect of temperature on the development of fracture process zone (FPZ)

In the three-point bending test of the SCB specimen, a stress concentration zone above the notch tip was identified, exhibiting nonlinear deformation under loading [25], [60]. Commonly referred to as FPZ, this area represents a crucial fracture characteristic of rocks. To investigate the impact of high temperature treatment on the development of FPZ, a DIC technique was used to record the deformed images of SCB samples under mixed mode I/II loading condition. A specific region, referred to as the ROI as depicted in Fig. 2a, was selected to obtain full-field displacement and maximum principal strain results during mixed mode I/II loading using DIC analysis. Figures 5, 6 and 7 show the horizontal displacement and maximum principal strain of ROI at different stages during the mixed mode I/II loading process for SCB samples treated at 200 °C, 600 °C and 1000 °C respectively. In

order to enhance clarity in visualizing the progression of crack growth, a maximum principal strain range of 0 to 0.01 was selected for all samples. This range effectively captures the strain fluctuations and microcracking patterns in rocks prior to failure [48], [61]. The red zone in the maximum principal strain contours indicates areas with elevated strain values, providing an approximate indication of the direction of crack propagation (Figs. 5, 6 and 7).

A comprehensive comparison of Figs. 5, 6 and 7 reveals that SCB specimens treated at different temperatures show different microcracking behavior, which indicates that temperature has an impact on the fracture behavior at micro-scale under mixed mode I/II loading. Under pure mode I loading, horizontal displacement exhibited symmetrical distribution concerning the vertical notch extension direction of SCB samples [3], [26], [27], [32]. However, with the shift to mixed mode I/II loading, the distribution of horizontal displacement altered, with the symmetry axis deflecting in alignment with crack propagation direction. The displacement at the initial loading stage was related to the microcrack initiation. For example, for the SCB specimen after 200 °C treatment, a localized strain concentration near the notch tip was observed at load of 85% P_{max} (Fig. 5e). When the temperature increases to 1000 °C, crack initiation occurs at load of 60% P_{max} (Fig. 7e). This shows that high temperature treatment can reduce the crack initiation stress level of rocks, which is consistent with the results of previous experimental results on rocks under uniaxial compression loading [62], [63]. Given the high temperature treatment, there is an increase in both the quantity and size of microcracks, thereby facilitating the stages of crack initiation, propagation, and coalescence. This observation aligns with previous findings by Eberhardt et al. [64], indicating a significant reduction in crack initiation stress with heightened levels of sample damage.

With increasing load, the convergence of horizontal displacement contours becomes more pronounced, indicating crack development (e.g., Fig. 6c and 7c), as evident in the distribution of maximum principal strain (e.g., Fig. 6g and 7g). At 100% P_{max}, significant crack growth occurs on SCB specimens (Figs. 5h, 6h and 7h). While macroscopic fracture analysis indicates minimal temperature influence on specimen failure mode (Fig. 4), micro-scale crack features revealed by maximum principal strain contours obtained by DIC analysis highlight the significant impact of high temperature treatment on microcracking behavior of rocks. For example, as the temperature increases, the microcrack morphology (red areas in Figs. 5h, 6h and 7h) changes significantly, with microcrack size gradually increasing with elevated heating temperature. The length of crack at 1000 °C (Fig. 5h)

significantly exceeds that observed at 200 °C (Fig. 7h), suggesting heightened rock damage due to high temperature treatment. This phenomenon was also observed in the SCB specimens after high temperature treatment under pure mode I loading [31], [32] and pure mode II loading [48].

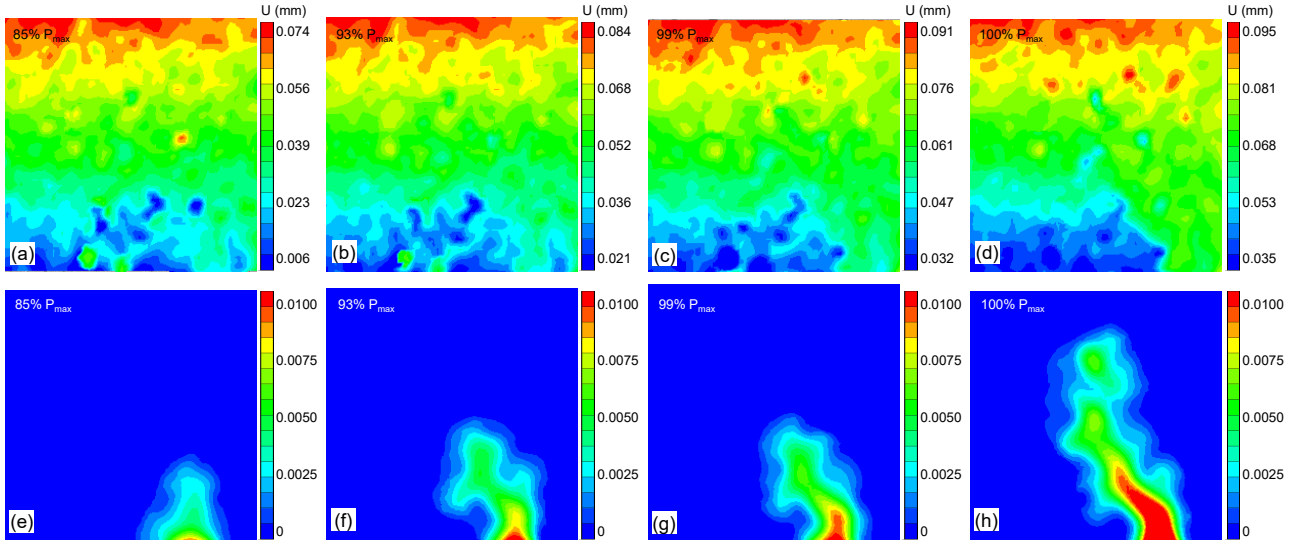

Fig. 5 Evolution of horizontal displacement and maximum principal strain contours of SCB samples under different loading stages at 200 °C: **a**~**b** horizontal displacement; **e**~**h** maximum principal strain. P_{max} represent the peak load.

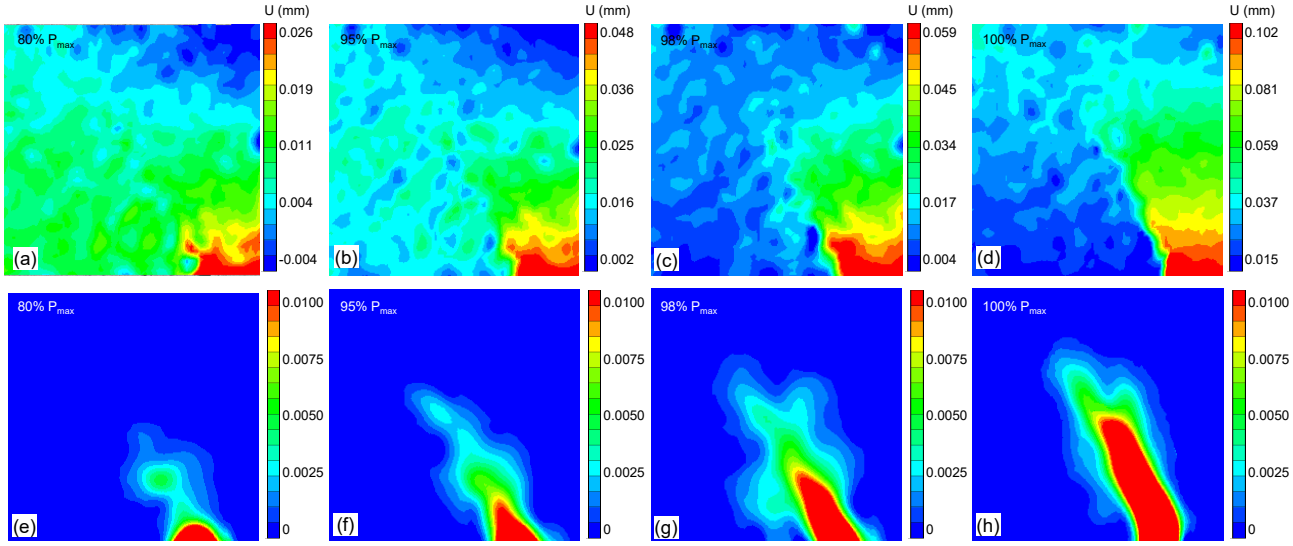

Fig. 6 Evolution of horizontal displacement and maximum principal strain contours of SCB samples under different loading stages at 600 °C: **a**~**b** horizontal displacement; **e**~**h** maximum principal strain. P_{max} represent the peak load.

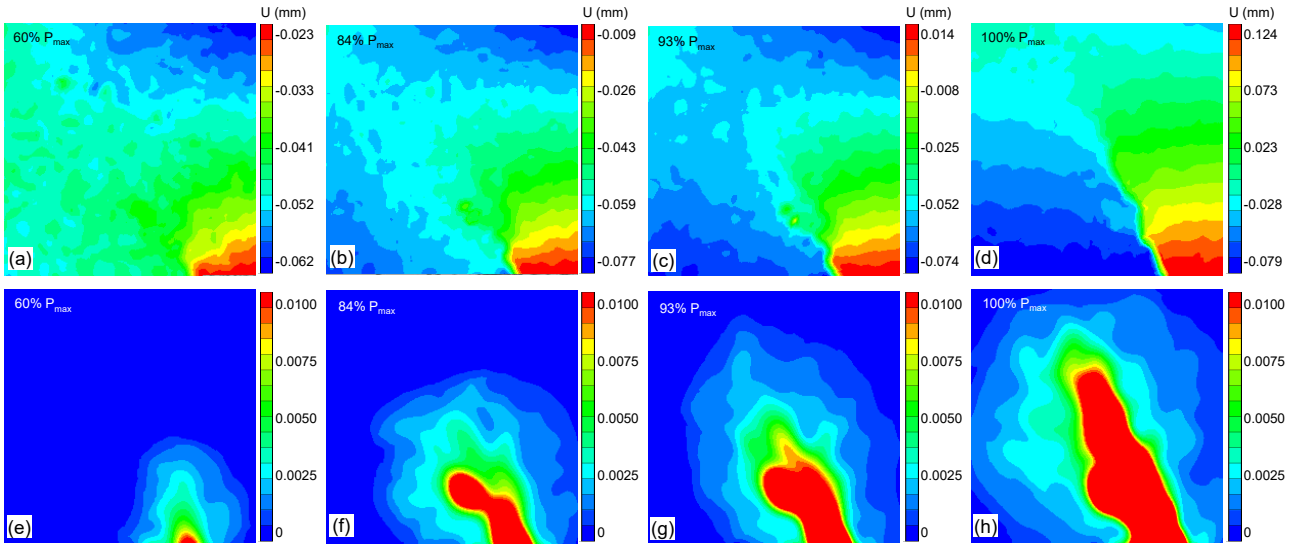

Fig. 7 Evolution of horizontal displacement and maximum principal strain contours of SCB samples under different loading stages at 1000 °C: **a**~**b** horizontal displacement; **e**~**h** maximum principal strain. P_{max} represent the peak load.

The evolution of FPZ at the notch tip progresses with increasing load and plays a pivotal role in the rock fracture mechanism. To quantitatively analyze the evolution of FPZ, a direct and accurate method relies on assessing alterations in the displacement field surrounding the notch tip obtained by DIC analysis [3], [26], [36], [38], [65]. The FPZ is considered fully developed at peak load, extending from the notch tip to the point where displacement discontinuity occurs, identified by the merging of displacement contours [66]. In contrast to pure mode I loading condition, the mixed mode I/II loading reveals a notable angular deviation between the crack initiation position of the SCB specimen and the notch tip direction. To facilitate FPZ size measurement at peak load, a new coordinate system is introduced at the notch tip, with the main crack initiation angle as the reference (Fig. 8a) [33], [65]. The coordinate transformation equations are given as follows [65]:

$$U_1 = U\cos\alpha - V\sin\alpha \tag{9}$$

$$V_1 = U\sin\alpha - V\cos\alpha \tag{10}$$

where α represents the initial crack initiation angle of the main crack, and this parameter can be measured by the program ImageJ; U and V represent the original horizontal displacement and vertical displacement respectively.

The following will introduce the FPZ analysis process using SCB samples treated at 1000 °C as an example. As shown in Fig. 8a, a set of horizontally distributed reference lines (y_1, y_2, y_3…y_n) was

414 initially positioned along the positive Y-axis above the crack path in the new coordinate system, with
415 monitoring of the horizontal displacements U_1 at peak load and X-coordinates of these reference lines.
416 The FPZ width (W_{FPZ}) is determined by the horizontal length of the region exhibiting a notable
417 horizontal displacement gradient. As shown in Fig. 8b, as the horizontal reference line approaches the
418 notch tip, distinct horizontal displacement jumps are observed. For example, the reference line y=3.2
419 mm shows a large jump and the horizontal length of this region is 4.25 mm (W_{FPZ}=4.25 mm). Two
420 vertical reference lines in the new coordinate system (left and right lines in Fig. 8a) were
421 symmetrically laid out at two sides of crack path to obtain the evolution of horizontal displacement
422 with Y-coordinates (Fig. 8a). The FPZ length (L_{FPZ}) is determined as the distance from the notch tip to
423 the point along the crack ligament where the displacement jump vanishes at peak load. Additionally,
424 the CTOD (W) is obtained by calculating the difference in horizontal displacement on both sides of
425 the notch tip, with its value at peak load identified as the critical CTOD (W_c). These methods of
426 obtaining FPZ shape parameters (W_{FPZ} and L_{FPZ}) and CTOD from horizontal displacement contours
427 have been previously validated [3], [24], [27], [67], [68]. Based on the evolution of horizontal
428 displacement with Y-coordinates in Fig. 8c, the values of L_{FPZ} and W_c of SCB sample after 1000 °C
429 treatment are computed to be 14.14 mm and 0.215 mm, respectively. Fig. 8d shows the horizontal
430 displacement of SCB sample after 1000 °C treatment under different loading stages along the two
431 vertical reference lines. The CTOD value increases from 0.011 mm at 60 % P_{max} to 0.058 mm at 93%
432 P_{max}, and the critical CTOD at peak load is 0.215 mm. As loading proceeds, the value of CTOD also
433 increases, which is consistent with the results observed in SCB samples under pure mode I loading
434 [32]. Notably, the relationship between load and CTOD value is nonlinear, with the CTOD value
435 increasing more rapidly as the load approaches the peak, indicating the nonlinear damage behavior of
436 rock under mixed mode I/II loading. Similarly, the opening displacement is not precisely zero at the
437 FPZ tip due to slight deviations in the positioning of the selected vertical reference lines relative to the
438 fracture surfaces (Figs. 8c and 8d).

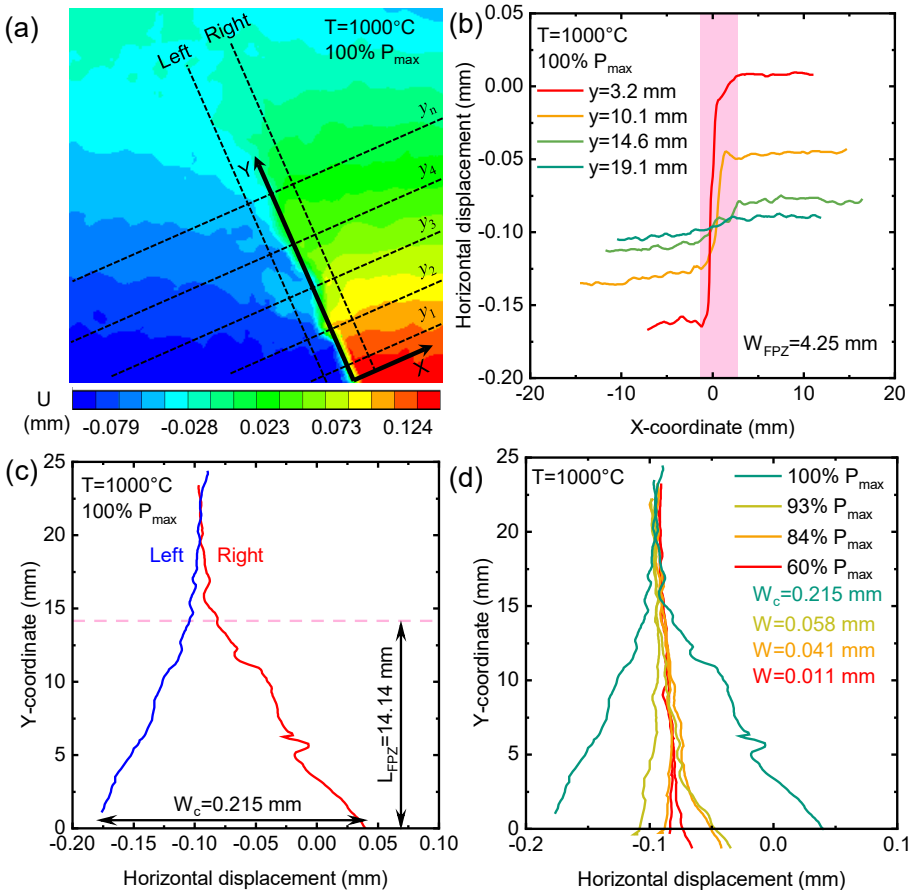

Fig. 8 FPZ analysis process of pre-heated SCB samples at 1000 °C: **a** horizontal and vertical reference lines in the new coordinate system in horizontal displacement contours; **b** horizontal displacement changes at different horizontal reference lines; **c** horizontal displacement curves along the vertical reference lines; **d** CTOD values under different loading stages.

Comparison of the lengths, widths of the FPZ, and critical CTOD values at peak load were conducted for SCB samples subjected to various high-temperature treatments under mixed mode I/II loading conditions, as depicted in Fig. 9a. While not strictly monotonic, an overall trend reveals an increase in both FPZ length and width with temperature. As the temperature increases from 200 to 1000 °C, the FPZ length increases from 4.93 to 14.14 mm, which is an increase of approximately 2.87 times, and the FPZ width expanded from 1.93 to 4.25 mm, indicating an increase of about 2.20 times. Notably, the critical CTOD (W_c) value appears highly responsive to temperature variations. As the temperature increases from 200 to 1000 °C, the value of W_c increases from 0.023 to 0.215 mm, marking a remarkable increase of approximately 9.35 times. In addition, these parameters and fracture toughness all show a negative correlation. It seems that as the temperature increases, the length and width of the FPZ also increase and the value of the fracture toughness decreases. This conclusion was also confirmed in the experiments of pre-heated SCB specimens under pure mode I

loading [31], [32] and pure mode II loading [65].

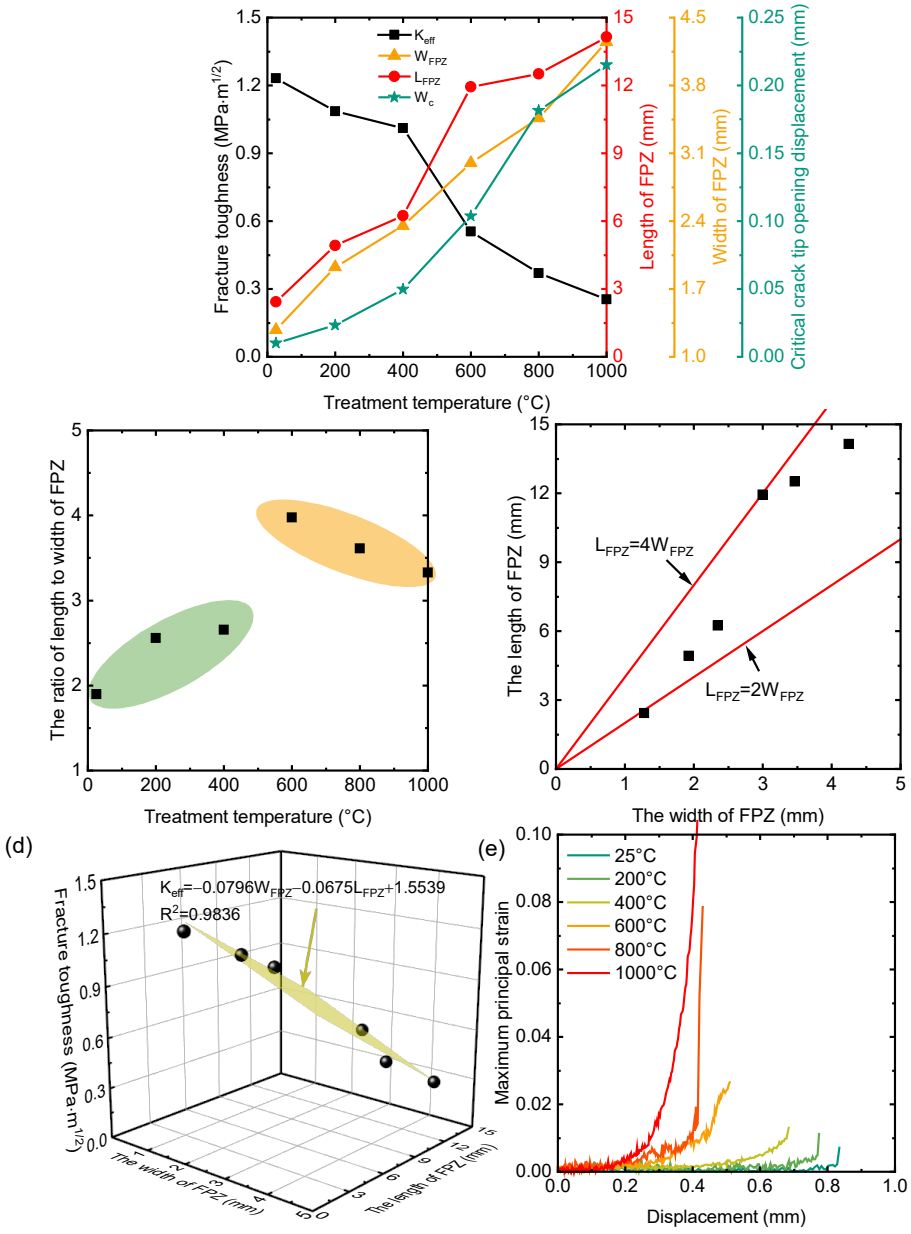

Fig. 9 Evolution of FPZ parameters and maximum principal strain: **a** the development of FPZ length, FPZ width, critical crack tip opening displacement and fracture toughness with temperature at peak load; **b** the ratio of length to width of FPZ under different temperatures; **c** relationship between FPZ length and width; **d** relationship between FPZ geometric parameters and fracture toughness; **e** evolution of maximum principal strain at the notch tip.

The ratio of FPZ length to width reflects its shape, which is of great significance for studying the progressive damage process of rocks and relevant theoretical frameworks [30]. The relationship between the FPZ length and width of the pre-heated SCB specimen under mixed mode I/II loading is shown in Figs. 9b and 9c. It is evident that the ratio of FPZ length to width in all specimens

predominantly fell within the 2~4 range, which was consistent with the results of previous works [30], [69], [70]. At lower temperatures (25~400 °C), the ratio remains around 2~3, while at higher temperature (600~1000 °C), this value increases to 3~4. This is consistent with the effect of temperature on the effective fracture toughness (Fig. 3d). Within the 400~600 °C range, there is a brittle-ductile transition phenomenon in the rock, which leads to a great change in the shape of the FPZ, markedly altering the FPZ shape from a semi-elliptical to a gradually narrowing region. Previous research has confirmed that the aspect ratio of FPZ is related to many factors, such as sample dimensions and rock properties [30], [69], [70]. The present experimental results suggest that temperature is another important factor influencing the FPZ shape. Utilizing the DIC technique to ascertain FPZ shape from the sample surface technically delineates the development of the inelastic or damage zone within the rock, given the anticipated uniformity of FPZ along the crack front [30], [71]. As shown in Fig. 9d, a discernible mathematical relationship exists between FPZ length, width, and the effective fracture toughness of SCB samples, offering a practical method for forecasting the latter under mixed mode I/II loading conditions. Therefore, the results of this work contribute to a quantitative understanding of the nonlinear evolution of the damage zone in rocks subjected to mixed mode I/II loading. It is worth noting that the measured FPZ length at room temperature (2.43 mm) in this study is smaller than previous findings [30], [46], [72], [73]. For example, Ma et al. [73] obtained that the FPZ length of fine-grained quartz-diorite SCB sample was 6.6 mm under pure mode I loading. Conversely, a broader FPZ length (~8–10 mm) was observed by Wei et al. [72] in a SCB test of Dazhou sandstone. Such discrepancies underscore the multitude of factors influencing FPZ size, including loading conditions, rock types, and external environmental variables. Therefore, the FPZ size identified in this work can only be used in the theoretical predictions of fracture behaviors for SCB samples with identical rock type and geometry under mixed mode I/II loading.

The variation in maximum principal strain within the FPZ throughout the loading process serves as a reflection of the rock damage evolution [26]. To quantitatively analyze the maximum principal strain within FPZ changes during mixed mode I/II loading process, the maximum principal strain at the notch tip is continuously monitored and the results of different pre-heated SCB samples are shown in Fig. 9e. It shows that after high-temperature treatment, the initiation of thermally induced cracks in rocks will intensify the damage evolution process of rocks under mixed mode I/II loading. At lower temperatures (25~400 °C), the maximum principal strain development goes through a low strain

period, and then its value increases rapidly after reaching a certain point until the sample failure. At higher temperatures (600~1000 °C), the strain increases rapidly with increasing displacement. Particularly noteworthy are the SCB samples subjected to temperatures of 800 and 1000 °C, where significant strains are evident even under minimal displacement, indicating the ductile behavior of rocks under extremely high temperatures [48]. The results in Fig. 9e also show that the value of maximum principal strain obtained by DIC technique, like the AE counts [27], [32], [35], can also quantitatively characterize the damage process of rock, which provides a potential way for further establish the damage constitutive models of pre-heated rocks.

4. Discussion

Rock is a quasi-brittle and heterogeneous material, and its mechanical behavior is influenced by the microscopic internal structure response. The initiation and propagation of microcracks caused by thermal stress will cause irreversible damage to the rock microstructure. The experimental results in this work indicate that the microstructural changes induced by the high temperature treatment have a significant impact on the evolution of mixed mode I/II fracture characteristics of SCB samples, including effective fracture toughness and absorbed energy (Fig. 3), macroscopic fracture characteristics (Fig. 4), the development of FPZ, CTOD and maximum principal strain (Fig. 9).

Qualitative observation of the microscopic fracture morphology of pre-heated rocks at the grain-scale was conducted using SEM technique to elucidate the micro-mechanism of temperature impact on mixed mode I/II fracture. The SEM images of different pre-heated samples are presented in Fig. 10. The examination revealed that at room temperature, the fracture surface of the rock sample appeared nearly intact and flat, with minimal pre-existing microcracks (Fig. 10a). When increasing the temperature to 200 °C, the step pattern was observed (Fig. 10b). This is attributed to material separation along a series of crystal planes of varying heights rather than a singular plane, leading to stepped fractures [19]. At the same time, thermally induced cracks begin to initiates, including intragranular (IG) and grain boundary (GB) cracks. It is difficult to precisely identify the sequence of initiation of the two types of cracks in experiments. Given that the mechanical properties of grain boundaries are typically weaker and more heterogeneous than those of mineral grains in rocks [74], GB cracks appeared to predominate on the fracture surfaces at lower temperatures. As the

temperature increased further, an increased presence of microcracks was observed, facilitating the formation of interconnected network of microcracks. (Fig. 10c). When increasing the temperature to 600 °C, fragmented grain gradually appears, which is a volume damage zone caused by highly interconnected microcracks (Fig. 10d). It indicates that the thermal damage to the internal structure of the rock has reached a relatively high level. The fragmentation of these grains compromised the integrity of the rock microstructure, resulting in a significant reduction in fracture toughness (Fig. 3d). Continuing the temperature rise to 800 °C, individual fragmented grains further deteriorated, resulting in numerous broken grains and a decline in rock mechanical properties (Fig. 10e). At a temperature of 1000 °C, numerous microcracks become observable, culminating in the formation of an intricate network of cracks. Furthermore, discernible evidence of mineral grain surface melting is evident (Fig. 10e). This was also observed in microphotographs from previous studies on high temperature treated granite [14].

Additionally, the microcrack width was quantified using ImageJ (Figs. 10d~10f). When the temperature increases from 600 to 1000 °C, the microcrack width (aperture) increases from 1.228 μm to 3.783 μm, resulting in an increase of approximately 3.08 times. Previous studies have shown that an increase in microcrack width may brought about a remarkably greater contribution to the permanent strain than the increase of the crack density [75]. This increase in microcrack density and width is considered to be the important reason for the increase in rock porosity after high temperature treatment [54], [76], [77]. This change in rock microstructure caused by temperature will also be reflected in the load-displacement curve. When the temperature is lower (e.g., 200 °C), there is almost no initial nonlinear compaction stage in the load-displacement curve (Fig. 3a), and the size of FPZ was relatively small (Fig. 9). When the temperature is higher (e.g., 800 °C), the initial compaction stage becomes obvious, and both pre-peak hardening and post-peak softening stage are more significant (Fig. 3a), and an enlarged FPZ size (Fig. 9), indicating that the pre-heated rock has obvious ductility characteristics.

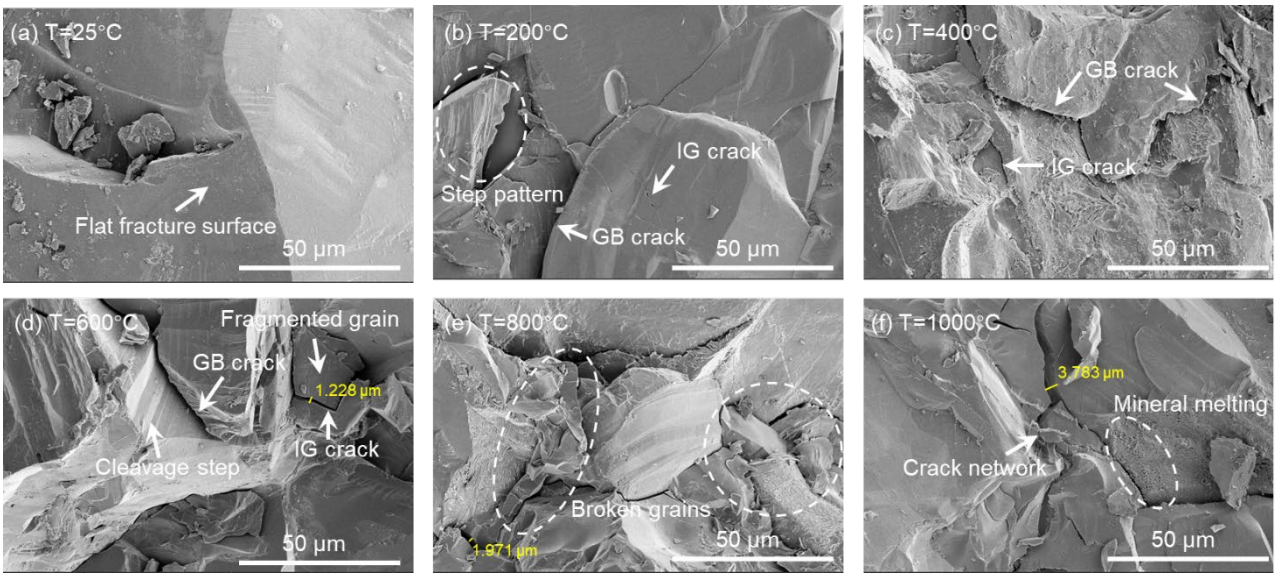

Fig. 10 Micrographs of fracture surface topography of rocks under different temperatures: **a** 25 °C; **b** 200 °C; **c** 400 °C; **d** 600 °C; **e** 800 °C; **f** 1000 °C. The solid yellow lines in **d**, **e** and **f** represent the measured crack width. The areas shown were chosen independently of the evolution of the fracture process, and do not necessarily correspond to a specific failure pattern.

Observation of the effects of high temperature treatment on rock microstructure can be facilitated through polarization microscopy. The results of microscopic observation under cross-polarized (Figs. 11a~11c) and plane-polarized (Figs. 11d~11f) light conditions are similar to those observed by SEM (Fig. 10). There are some pre-existing microcracks in rocks at room temperature (Fig. 11d), which are one of the causes of the initial nonlinear stage in the load-displacement curve. Elevated temperatures induce nonuniform expansion among mineral grains within rocks, arising from disparate thermal expansion coefficients inherent to distinct mineral types, thereby precipitating the generation of thermally induced cracks. With increasing temperature regimes, the number of such thermally induced cracks increases correspondingly (Figs. 11e and 11f). Even though the main component of the rocks investigated in this work is albite, there may still be mismatches between minerals of the same type due to the anisotropy and heterogeneity of single minerals [78], [79]. In contrast to samples at room temperature conditions, samples subjected to thermal treatment typically exhibit a stochastic distribution of thermally induced cracks, consequently leading to diminished energy expenditure during rock fracturing [39]. The thermally induced cracks in the pre-heated samples will connect, aggregate, and expand with pre-existing cracks and newly-formed cracks around the notch tip under mixed mode I/II loading, ultimately contributing to the increase in FPZ size (including width and

length).

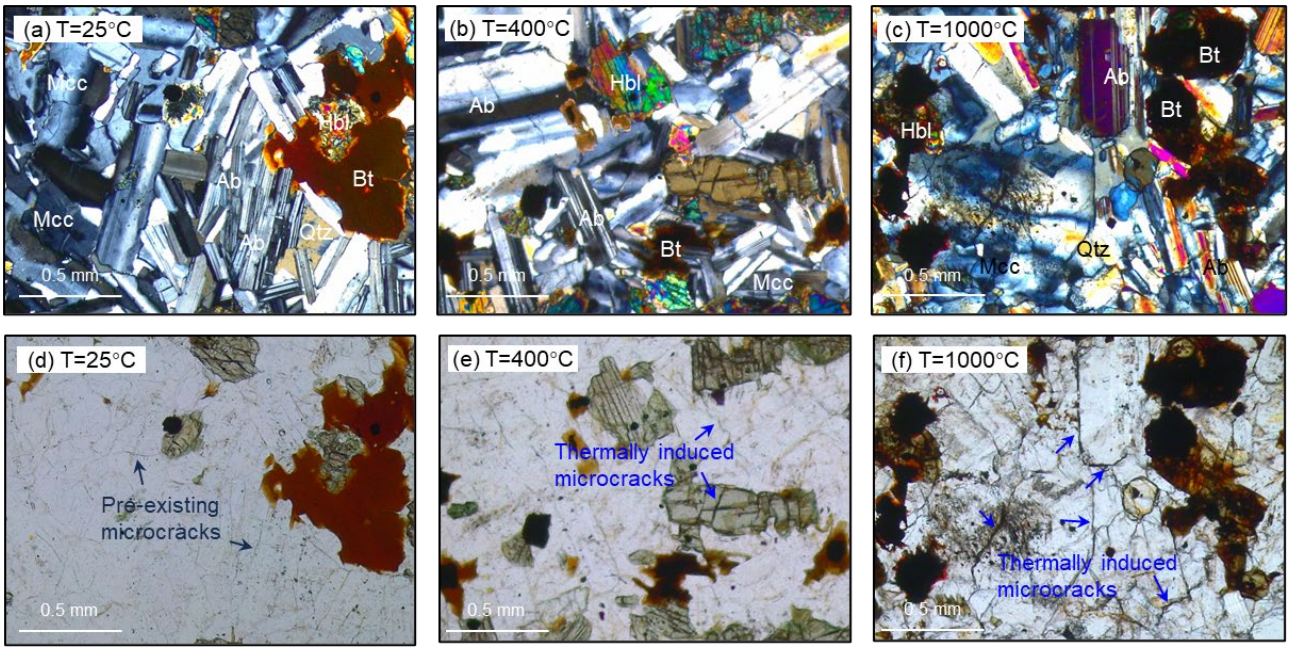

Fig. 11 Thin-section microphotographs of thin section of rocks under different temperatures: **a**~**c** images in cross-polarized light at 25 °C, 400 °C and 1000 °C, respectively; **d**~**f** images in plane-polarized light at 25 °C, 400 °C and 1000 °C, respectively. **a**/**d**, **b**/**e**, and **c**/**f** represent microphotographs of the same area. Qtz: quartz, Mcc: microcline, Hbl: hornblende, Bt: biotite, Ab: albite.

The nonlinear evolution of the FPZ at the notch tip of SCB specimens theoretically consists of four stages (stage I, stage II, stage III and stage IV), which has been summarized by previous works and confirmed in the laboratory tests by different techniques such as DIC, AE and computed tomography [25], [29], [80], [81], as shown in Figs. 12a and 12b. For example, in stage III, observable deformations arise directly due to microcrack coalescence and the emergence of mesocracks (also known as dominant microcracks) within the FPZ. According to the findings of this work, the process of FPZ development in rocks is expedited by high-temperature treatment compared to rocks at room temperature. As shown in Fig. 12c, in the SCB specimen after high temperature treatment under mixed mode loading, the presence of thermally induced cracks facilitates the coalescence of microcracks, thereby enabling the formation of mesocracks in stage II', consequently leading to the expansion of the FPZ size. The significant FPZ size obtained for pre-heated SCB samples in this work (Fig. 9 and Fig. 12c) demonstrates the development of a substantial nonlinear damage zone ahead of the notch tip. Furthermore, in contrast to pure mode I loading, the FPZ development process within specimens under mixed mode loading may exhibit more nonlinear and

intricate characteristics. Hence, linear elastic fracture mechanics might not be applicable to such samples, given the extensive nonlinear deformation within the samples under mixed mode I/II loading.

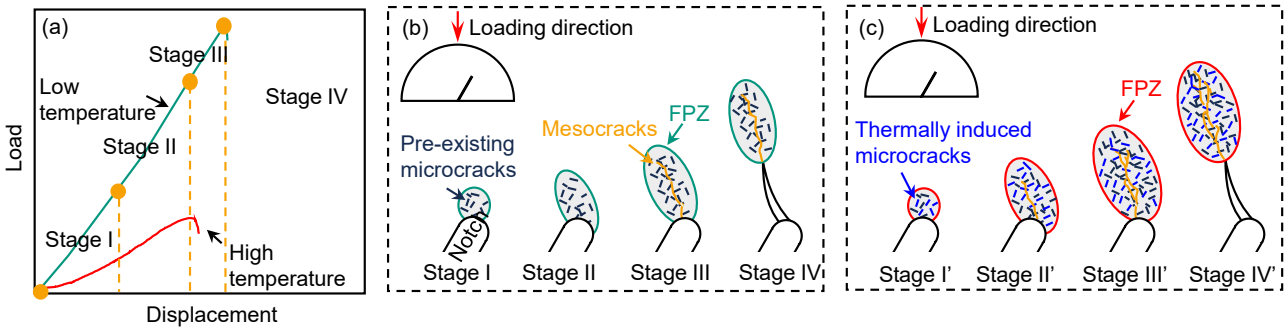

Fig. 12 The development of FPZ and mechanical behavior of SCB samples after different temperature treatments under mixed mode I/II loading: **a** load-displacement curves of SCB samples; **b** the development of FPZ at low temperature; **c** the development of FPZ at high temperature.

The importance of temperature in determining the fracture toughness and FPZ properties of rocks under mixed mode I/II loading is highlighted in this work, although other factors, including loading conditions [16], anisotropy [30], rock type [82] and sample size [83], [84], also affect the fracture toughness and FPZ properties of rocks, which warrant further investigation. Future investigations will entail the aggregation of a substantial corpus of experimental findings concerning rock fracture toughness and properties of the FPZ) achieved through analogous experimental inquiries encompassing diverse rock mineralogical compositions, sample configurations, and loading conditions. As an important tool in the field of geotechnical engineering, theoretical models play an indispensable role in the design of engineering stability [85], [86], [87]. Thereafter, a consolidated theoretical framework integrating these variables in conjunction with temperature effects will be established, aiming to explicate the alterations in rock fracture properties ensuing high temperature exposures. Especially in some deep underground rock engineering projects, such as nuclear waste repositories and geothermal reservoirs, this unified theoretical model that includes temperature will greatly facilitate more accurate design of support structures of those rock engineering.

5. Conclusions

This study experimentally investigates the fracture behavior of rocks after high temperature treatments under mixed mode I/II loading. Specifically, the characteristics of FPZ were analyzed

using DIC method. Detailed microscopic analysis of fracture surface morphology was performed to study the underlying mechanisms governing changes in the mechanical properties and fracture behavior of rocks after high temperature treatment. The main findings are outlined as follows:

(1) As the temperature increases, the mechanical properties of the SCB samples gradually decrease. Compared to samples at room temperature, rocks treated with temperature above 600 °C showed a notable decrease in peak load, generalized stiffness, fracture toughness, and absorbed energy. The load-displacement curves and macroscopic fracture characteristics of pre-heated SCB samples exhibit a transition from brittleness to ductility with increasing temperature under mixed mode I/II loading.

(2) The length and width of FPZ increased with increasing temperature, and the CTOD values of pre-heated samples increased with increasing loading level. These parameters exhibit an inverse relationship with fracture toughness. The ratio of FPZ length to width of all samples predominantly ranged between 2~4. At lower temperatures (25~400 °C), this ratio remained around 2~3, and when the temperature is higher (600~1000 °C), its value increased to 3~4. A robust mathematical correlation exists between FPZ dimensions and fracture toughness, offering a practical method for predicting the effective fracture toughness of pre-heated rocks under mixed mode I/II loading.

(3) The initiation of thermally induced cracks in rocks will intensify the damage evolution of rocks under mixed mode I/II loading. At lower temperatures ranging from 25 to 400 °C, the evolution of maximum principal strain initially undergoes a phase of subdued strain, followed by a swift escalation in maximum principal strain beyond a critical threshold, culminating in sample failure. At higher temperatures (600~1000 °C), the strain increases rapidly with increasing displacement. Particularly in SCB samples heated to 800 and 1000 °C, substantial strains are observed even under minimal displacement, indicative of the ductile property of rocks at extremely high temperatures.

(4) Both SEM and polarization microscopy images reveal the microscopic fracture morphology of pre-heated rocks, showing isolated and dispersed microcracks at lower temperatures and microcrack networks with broken grains at higher temperatures. The interconnected network of microcracks and fragmented grains compromises rock integrity, leading to an increase in FPZ size and a reduction in fracture toughness.

In summary, this study emphasizes the impact of high temperature treatment on the mechanical attributes and characteristics of FPZ in rocks subjected to mixed mode I/II loading. It demonstrates

646 that temperature significantly impacts effective fracture toughness, maximum principal strain
647 distribution, and FPZ geometric parameters of rocks. Consequently, thermal damage warrants
648 comprehensive consideration in theoretical models and numerical simulations pertinent to deep
649 underground rock engineering.
650

Declaration of Competing Interest

The authors declare that they have no known competing financial interests or personal relationships that could have appeared to influence the work reported in this paper.

Data Availability Statements

All data generated or analyzed during this work are included in this published paper and are available from the corresponding author on reasonable request.

Acknowledgements

This research was supported by the National Natural Science Foundation of China (51778575). The sponsorship guaranteed with basic research funds provided by Politecnico di Torino, Italy, for its financial aid in this work is also acknowledged. The authors sincerely thank Dr. Leguang Li at the School of Earth Sciences in China University of Geosciences (Wuhan) for his valuable assistance during the thin-section petrographic tests. The authors sincerely thank Dr. Yang Yang at the School of Materials Science and Engineering in Zhejiang University for her kindly help during the semi-circular bending tests. In addition, the first author wants to express his acknowledgment to the China Scholarship Council (CSC) for providing financial support to study at Politecnico di Torino, Italy.

References

[1] Tran, N. H., & Rahman, S. S. (2007). Development of hot dry rocks by hydraulic stimulation: Natural fracture network simulation. Theoretical and Applied Fracture Mechanics, 47(1), 77-85.

[2] Shen, Q. Q., Rao, Q. H., Sun, D., Yi, W., Huang, D., & Li, Z. (2022). A new optimization method of double-crack distributions for improving network fracture conductivity of natural gas exploitation. Theoretical and Applied Fracture Mechanics, 122, 103655.

[3] Zhang, C., Li, D., Zhou, A., Ru, W., Zhu, Q., & Ma, J. (2024). Effect of loading rate on mode I fracture behavior of red sandstone: Insights from AE and DIC techniques. Theoretical and Applied Fracture Mechanics, 104364.

[4] Yin, T. B., Shu, R. H., Li, X. B., Pin, W. A. N. G., & Liu, X. L. (2016). Comparison of mechanical properties in high temperature and thermal treatment granite. Transactions of Nonferrous Metals Society of China, 26(7), 1926-1937.

[5] Wong, L. N. Y., Zhang, Y., & Wu, Z. (2020). Rock strengthening or weakening upon heating in the mild temperature range. Engineering Geology, 272, 105619

[6] Miao, S., Pan, P. Z., Zhao, X., Shao, C., & Yu, P. (2021). Experimental study on damage and fracture characteristics of Beishan granite subjected to high-temperature treatment with DIC and AE techniques. Rock Mechanics and Rock Engineering, 54, 721-743.

[7] Hu, X., Shentu, J., Xie, N., Huang, Y., Lei, G., Hu, H., ... & Gong, X. (2023a). Predicting triaxial compressive strength of high-temperature treated rock using machine learning techniques. Journal of Rock Mechanics and Geotechnical Engineering, 15(8), 2072-2082.

[8] Fowell RJ (1995) Suggested method for determining mode I fracture toughness using Cracked Chevron Notched Brazilian Disc (CCNBD) specimens. Int J Rock Mech Min Sci 32(1):57–64.

[9] Kuruppu MD, Obara Y, Ayatollahi MR, Chong KP, Funatsu T (2014) ISRM-suggested method for determining the mode I static fracture toughness using semi-circular bend specimen. Rock Mech Rock Eng 47(1):267–274.

[10] Kang, P., Hong, L., Zou, Q., Wen, Z., & Zhang, Y. (2020). Evolutionary characteristics of mode-I fracture toughness and fracture energy in granite from different burial depths under high-temperature effect. Engineering Fracture Mechanics, 239, 107306.

[11] Ge, Z., Sun, Q., Yang, T., Luo, T., Jia, H., & Yang, D. (2021). Effect of high temperature on mode-I fracture toughness of granite subjected to liquid nitrogen cooling. Engineering Fracture Mechanics, 252, 107834.

[12] Hu, X., Liao, D., Ma, D., Xie, S., Xie, N., Hu, H., & Gong, X. (2023). Machine learning models for predicting rock fracture toughness at different temperature conditions. Case Studies in Construction Materials, 19, e02622.

[13] Feng G, Kang Y, Meng T, Hu YQ, Li XH (2017) The Influence of temperature on mode I fracture toughness and fracture characteristics of sandstone. Rock Mech Rock Eng 50:2007–2019

[14] Sun, Q., Zhang, W., Zhu, Y., & Huang, Z. (2019). Effect of high temperatures on the thermal properties of granite. Rock Mechanics and Rock Engineering, 52, 2691-2699.

[15] Funatsu, T., Kuruppu, M., & Matsui, K. (2014). Effects of temperature and confining pressure on mixed-mode (I–II) and mode II fracture toughness of Kimachi sandstone. International Journal of Rock Mechanics and Mining Sciences, 67, 1-8.

[16] Feng, G., Kang, Y., Chen, F., Liu, Y. W., & Wang, X. C. (2018). The influence of temperatures on mixed-mode (I+ II) and mode-II fracture toughness of sandstone. Engineering Fracture Mechanics, 189, 51-63.

[17] Kang, P., Hong, L., Yan, F., Zou, Q., Xiao, S., & Liu, Z. (2020). Effects of temperature on mechanical properties of granite under different fracture modes. Engineering Fracture Mechanics, 226, 106838.

[18] Suo, Y., Su, X., Ye, Q., Chen, Z., Feng, F., Wang, X., & Xie, K. (2022). The investigation of impact of temperature on mixed-mode fracture toughness of shale by semi-circular bend test. Journal of Petroleum Science and Engineering, 217, 110905.

[19] Yang, Y., Zhang, N., & Wang, J. (2022). Study on the Effect of Negative Temperature Change on the Fracture Morphology of Granite under Impact. Geofluids, 2022.

[20] Alneasan, M., & Alzo'ubi, A. K. (2023). Temperature effect on the fracture behavior of granite under three loading modes (I, I/II, and II). Rock Mechanics and Rock Engineering, 56(3), 2197-2211.

[21] Liu, L., Li, H., Li, X., Wu, D., & Zhang, G. (2021). Underlying mechanisms of crack initiation for granitic rocks containing a single pre-existing flaw: insights from digital image correlation (DIC) analysis. Rock Mechanics and Rock Engineering, 54, 857-873.

[22] Aboayanah, K. R., Abdelaziz, A., Haile, B. F., Zhao, Q., & Grasselli, G. (2024). Evaluation of Damage Stress Thresholds and Mechanical Properties of Granite: New Insights from Digital Image Correlation and GB-FDEM. Rock Mechanics and Rock Engineering, 1-28.

[23] Guy N, Seyedi DM, Hild F (2018) Characterizing fracturing of clay-rich lower watrous rock: from laboratory experiments to nonlocal damage-based simulations. Rock Mech Rock Eng 51:1777–1787.

[24] Zhang, S., Wang, H., Li, X., Zhang, X., An, D., & Yu, B. (2021). Experimental study on development

characteristics and size effect of rock fracture process zone. Engineering Fracture Mechanics, 241, 107377.

[25] Zhang, J. Z., & Zhou, X. P. (2022). Fracture process zone (FPZ) in quasi-brittle materials: Review and new insights from flawed granite subjected to uniaxial stress. Engineering Fracture Mechanics, 274, 108795.

[26] Wang, T., Sun, Q., Jia, H., Shen, Y., & Li, G. (2022). Fracture mechanical properties of frozen sandstone at different initial saturation degrees. Rock Mechanics and Rock Engineering, 55(6), 3235-3252.

[27] Xue, F., Lin, Z., & Wang, T. (2023). Experimental study on cracking process and fracture properties of granite under mode I loading by acoustic emission and digital image correlation. Fatigue & Fracture of Engineering Materials & Structures, 46(5), 1921-1936.

[28] Wu, X., Ma, L., Meng, T., Wang, Z., Zhao, G., Liu, P., & Taherdangkoo, R. (2024). The effect of fracture growth rate on the fracture process zone of salt rock after heat treatment. Engineering Fracture Mechanics, 110038.

[29] Munoz-Ibanez, A., Delgado-Martín, J., Herbón-Penabad, M., & Alvarellos-Iglesias, J. (2021). Acoustic emission monitoring of mode I fracture toughness tests on sandstone rocks. Journal of Petroleum Science and Engineering, 205, 108906.

[30] Dutler, N., Nejati, M., Valley, B., Amann, F., & Molinari, G. (2018). On the link between fracture toughness, tensile strength, and fracture process zone in anisotropic rocks. Engineering Fracture Mechanics, 201, 56-79.

[31] Zhang, X., Li, Z., Wang, X., Wang, H., Li, B., & Niu, Y. (2022). Thermal effect on the fracture behavior of granite using acoustic emission and digital image correlation: An experimental investigation. Theoretical and Applied Fracture Mechanics, 121, 103540.

[32] Chen, C., Chu, P., Xie, H., Li, M., Li, C., & Shang, D. (2023). Fracture behavior of high-temperature granite subjected to liquid nitrogen cooling: Semi-circular bending test and crack evolution analysis. Theoretical and Applied Fracture Mechanics, 128, 104100.

[33] Ji, W. W., Pan, P. Z., Lin, Q., Feng, X. T., & Du, M. P. (2016). Do disk-type specimens generate a mode II fracture without confinement? International Journal of Rock Mechanics and Mining Sciences, 87, 48-54.

[34] Wu, Y., Yin, T., Zhuang, D., Chen, Y., Ma, J., & Guo, W. (2023). Initial and unstable fracture toughness of quartz-diorite rock under mixed mode I/II loading: Experimental and numerical investigation. Theoretical and Applied Fracture Mechanics, 127, 104079.

[35] Suo, Y., Zhao, Y. J., Fu, X. F., He, W. Y., & Pan, Z. J. (2023). Research on the mixed-mode fracture damage characteristics of shale soaked in different drilling fluids. Geomechanics and Geophysics for Geo-Energy and Geo-Resources, 9(1), 156.

[36] Sun, W., Wu, S., & Guo, W. (2023). Study on the semi-circular bend method for characterizing the mixed mode I/II fracture toughness of sandstone: A micro-perspective. Theoretical and Applied Fracture Mechanics, 127, 104064.

[37] Zhu, Q., Li, D., Li, X., Han, Z., & Ma, J. (2023). Mixed mode fracture parameters and fracture characteristics of diorite using cracked straight through Brazilian disc specimen. Theoretical and Applied Fracture Mechanics, 123, 103682.

[38] Liang, X., Feng, G., Meng, T., Zhao, G., Wang, Z., Liu, P., & Taherdangkoo, R. (2024). Non-constant evolution of mixed mode fracture process zone in heat-treated salt rock during the whole loading. Theoretical and Applied Fracture Mechanics, 104337.

[39] Feng, Y., Su, H., Yu, L., Wu, C., & Wang, H. (2023). Mixed mode I-II fracture mechanism of sandstone samples after thermal treatment: Insights from optical monitoring and thermal analysis. Theoretical and Applied Fracture Mechanics, 125, 103883.

[40] Guo, T. Y., & Wong, L. N. Y. (2020). Microcracking behavior of three granites under mode I loading: Insights from acoustic emission. Engineering Geology, 278, 105823.

[41] Ayatollahi, M. R., & Aliha, M. R. M. (2007). Fracture toughness study for a brittle rock subjected to mixed mode I/II loading. International Journal of Rock Mechanics and Mining Sciences, 44(4), 617-624.

[42] Lim, I. L., Johnston, I. W., & Choi, S. K. (1993). Stress intensity factors for semi-circular specimens under three-point bending. Engineering Fracture Mechanics, 44(3), 363-382.

[43] Munoz, H., & Kiyota, T. (2020). Deformation and localisation behaviours of reinforced gravelly backfill using shaking table tests. Journal of Rock Mechanics and Geotechnical Engineering, 12(1), 102-111.

[44] Hedan, S., Valle, V., Giot, R., & Cosenza, P. (2022). Behavior in mixed-mode of desiccation cracks on a clayey rock front gallery. International Journal of Rock Mechanics and Mining Sciences, 154, 105104.

[45] Hebert, J., & Khonsari, M. (2023). The application of digital image correlation (DIC) in fatigue experimentation: A review. Fatigue & Fracture of Engineering Materials & Structures, 46(4), 1256-1299.

[46] Miao, S., Pan, P. Z., Yu, P., Zhao, S., & Shao, C. (2020). Fracture analysis of Beishan granite after high-temperature treatment using digital image correlation. Engineering Fracture Mechanics, 225, 106847.

[47] Sharafisafa, M., Aliabadian, Z., & Shen, L. (2020). Crack initiation and failure of block-in-matrix rocks under Brazilian test using digital image correlation. Theoretical and Applied Fracture Mechanics, 109, 102743.

[48] Su, H., Feng, Y., Zhang, Q., & Yu, L. (2022). Experimental study on the fracturing process of thermally treated granite under mixed mode I-II loading. Geomechanics and Geophysics for Geo-Energy and Geo-Resources,

787 8(2), 75.
788 [49] Gautam PK, Verma AK, Jha MK, Sharma P, Singh TN (2018) Effect of high-temperature on physical and
789 mechanical properties of Jalore granite. J Appl Geophys 159:460–474.
790 [50] Kang, F., & Li, Y. (2021). Grain size heterogeneity controls strengthening to weakening of granite over
791 high-temperature treatment. International Journal of Rock Mechanics and Mining Sciences, 145, 104848.
792 [51] Feng, G., Wang, X., Wang, M., & Kang, Y. (2020). Experimental investigation of thermal cycling effect on
793 fracture characteristics of granite in a geothermal-energy reservoir. Engineering Fracture Mechanics, 235,
794 107180.
795 [52] Darot, M., Gueguen, Y., Benchemam, Z., & Gaboriaud, R. (1985). Ductile-brittle transition investigated by
796 micro-indentation: results for quartz and olivine. Physics of the Earth and Planetary Interiors, 40(3), 180-186.
797 [53] Mahanta, B., Singh, T. N., & Ranjith, P. G. (2016). Influence of thermal treatment on mode I fracture toughness
798 of certain Indian rocks. Engineering Geology, 210, 103-114.
799 [54] Griffiths L, Heap MJ, Baud P, Schmittbuhl J (2017) Quantification of microcrack characteristics and
800 implications for stiffness and strength of granite. Int J Rock Mech Min Sci 100:138–150.
801 [55] Aliha, M. R. M., & Ayatollahi, M. R. (2011). Mixed mode I/II brittle fracture evaluation of marble using SCB
802 specimen. Procedia Engineering, 10, 311-318.
803 [56] Alneasan, M., & Behnia, M. (2021). An experimental investigation on tensile fracturing of brittle rocks by
804 considering the effect of grain size and mineralogical composition. International Journal of Rock Mechanics
805 and Mining Sciences, 137, 104570.
806 [57] Hu, X., Liao, D., Hu, H., Xie, S., Xie, N., & Gong, X. (2024). The Influence of Mechanical Heterogeneity of
807 Grain Boundary on Mechanical and Microcracking Behavior of Granite Under Mode I Loading Using a
808 Grain-Based Model. Rock Mechanics and Rock Engineering, 1-31.
809 [58] Hogan, J. D., Rogers, R. J., Spray, J. G., & Boonsue, S. (2012). Fracture and fragmentation of quartz and albite
810 during single-diamond sliding-point contact. Engineering Fracture Mechanics, 96, 165-178.
811 [59] Maruyama, I., Meawad, A., Kondo, T., Sawada, S., Halodova, P., Fedorikova, A., ... & Suzuki, K. (2023).
812 Radiation-induced alteration of sandstone concrete aggregate. Journal of Nuclear Materials, 583, 154547.
813 [60] Brooks, Z. (2013). Fracture process zone: Microstructure and nanomechanics in quasi-brittle materials
814 (Doctoral dissertation, Massachusetts Institute of Technology).
815 [61] Fakhimi A, Lin Q, Labuz JF (2018) Insights on rock fracture from digital imaging and numerical modeling. Int
816 J Rock Mech Min Sci 107:201–207

[62] Yao, M., Rong, G., Zhou, C., & Peng, J. (2016). Effects of thermal damage and confining pressure on the mechanical properties of coarse marble. Rock Mechanics and Rock Engineering, 49, 2043-2054.

[63] Kumari, W. G. P., Ranjith, P. G., Perera, M. S. A., Chen, B. K., & Abdulagatov, I. M. (2017). Temperature-dependent mechanical behaviour of Australian Strathbogie granite with different cooling treatments. Engineering Geology, 229, 31-44.

[64] Eberhardt, E., Stead, D., & Stimpson, B. (1999). Effects of sample disturbance on the stress-induced microfracturing characteristics of brittle rock. Canadian Geotechnical Journal, 36(2), 239-250.

[65] Meng, T., Wang, T., Guo, K., & Zhang, D. (2023). Study of mode II fracture characteristics and roughness in salt rock after treatment coupled thermo-hydro-mechanical environment. Engineering Fracture Mechanics, 291, 109572.

[66] Lilienthal, G. M., Zhong, Y., & Makhnenko, R. Y. (2023). Fracture process zone in crystalline rock: effect of specimen size and shape. Theoretical and Applied Fracture Mechanics, 128, 104118.

[67] Lin, Q., & Labuz, J. F. (2013). Fracture of sandstone characterized by digital image correlation. International Journal of Rock Mechanics and Mining Sciences, 60, 235-245.

[68] Wu, Y., Yin, T., Zhuang, D., Li, Q., & Chen, Y. (2022). Research on the effect of thermal treatment on the crack resistance curve of marble using notched semi-circular bend specimen. Theoretical and Applied Fracture Mechanics, 119, 103344.

[69] Tarokh A, Makhnenko RY, Fakhimi A, Labuz JF (2017) Scaling of the fracture process zone in rock. Int J Fract 204:191–204

[70] Wang, H., Ma, T., Liu, Y., Zhang, D., & Ranjith, P. G. (2024). Experimental investigation on the 3D anisotropic fracture behavior of layered shales under mode-I loading. Rock Mechanics and Rock Engineering, 1-24.

[71] Ghamgosar, M., & Erarslan, N. (2016). Experimental and numerical studies on development of fracture process zone (FPZ) in rocks under cyclic and static loadings. Rock Mechanics and Rock Engineering, 49, 893-908.

[72] Wei, M.D., Dai, F., Xu, N.W., et al., 2016. Experimental and numerical study on the fracture process zone and fracture toughness determination for ISRM-suggested semi-circular bend rock specimen. Eng. Fract. Mech. 154, 43–56.

[73] Ma, J., Li, D., Zhu, Q., Liu, M., & Wan, Q. (2022). The mode I fatigue fracture of fine-grained quartz-diorite under coupled static loading and dynamic disturbance. Theoretical and Applied Fracture Mechanics, 117, 103140.

[74] Tang X, Zhang Y, Xu J, Rutqvist J, Hu M, Wang Z, Liu Q (2022) Determining Young's modulus of granite using accurate grain-based modeling with microscale rock mechanical experiments. Int J Rock Mech Min Sci 157:105167.

[75] Lin, W. (2002). Permanent strain of thermal expansion and thermally induced microcracking in Inada granite. Journal of Geophysical Research: Solid Earth, 107(B10), ECV-3.

[76] Nasseri, M. H. B., Schubnel, A., & Young, R. P. (2007). Coupled evolutions of fracture toughness and elastic wave velocities at high crack density in thermally treated Westerly granite. International Journal of Rock Mechanics and Mining Sciences, 44(4), 601-616.

[77] Isaka, B. A., Ranjith, P. G., Rathnaweera, T. D., Perera, M. S. A., & De Silva, V. R. S. (2019). Quantification of thermally-induced microcracks in granite using X-ray CT imaging and analysis. Geothermics, 81, 152-167.

[78] Hu, X., Xie, N., Zhu, Q., Chen, L., & Li, P. (2020). Modeling damage evolution in heterogeneous granite using digital image-based grain-based model. Rock Mechanics and Rock Engineering, 1-21.

[79] Lamberson, L., & Ramesh, K. T. (2015). Spatial and temporal evolution of dynamic damage in single crystal α-quartz. Mechanics of materials, 87, 61-79.

[80] Jiang, R., Dai, F., Liu, Y., Li, A., & Feng, P. (2021). Frequency characteristics of acoustic emissions induced by crack propagation in rock tensile fracture. Rock Mechanics and Rock Engineering, 54, 2053-2065.

[81] Ghamgosar, M., Bahaaddini, M., Erarslan, N., & Williams, D. J. (2021). A new experimental approach to quantify microfractures in the Fracture Process Zone (FPZ) under various loading conditions. Engineering Geology, 283, 106024.

[82] Kramarov, V., Parrikar, P. N., & Mokhtari, M. (2020). Evaluation of fracture toughness of sandstone and shale using digital image correlation. Rock Mechanics and Rock Engineering, 53, 4231-4250.

[83] Ghouli, S., Bahrami, B., Ayatollahi, M. R., Driesner, T., & Nejati, M. (2021). Introduction of a scaling factor for fracture toughness measurement of rocks using the semi-circular bend test. Rock Mechanics and Rock Engineering, 54(8), 4041-4058.

[84] Li, J. L., Wei, X. D., & Zhao, G. F. (2023). An integrated experimental and numerical study of size effect on the mode I fracture toughness of rock. Engineering Fracture Mechanics, 287, 109327.

[85] Zhang, L., Zhang, D., Wang, Z., Cong, Y., & Wang, X. (2023). Constructing a three-dimensional creep model for rocks and soils based on memory-dependent derivatives: A theoretical and experimental study. Computers and Geotechnics, 159, 105366.

[86] Yu, Y., & Yang, Z. X. (2023). Bounding Surface Plasticity Model for Clay under Cyclic Loading Conditions

Considering Fabric Anisotropy. Journal of Engineering Mechanics, 149(9), 04023067.

[87] Yu, Y., & Yang, Z. (2023). Bounding surface rotational hardening model for overconsolidated clay accounting for evolving fabric anisotropy. International Journal for Numerical and Analytical Methods in Geomechanics, 47(3), 370-391.